The equations for δ^{I} and δ^{II} may be written in numerical form:

$$\delta^{I}=\frac{1-(r_i/r_h)^5}{2.66-7(r_i/r_h)^5} \tag{A14}$$

and

$$\delta^{II}=\frac{1-(r_i/r_h)^5}{1-7(r_i/r_h)^5}. \tag{A15}$$

Using these expressions and Eq. (A6b) we determine for the Zn-II resonance a strain-induced frequency shift of $\sim$18 MHz compared to the observed value of $\sim$10 MHz. Evidently these small impurity-induced strains are more than sufficient to explain the observed shifts, however, a more comprehensive theory which properly includes the relaxation of the crystal and F^{-}-F^{-} repulsion appears necessary.

PHYSICAL REVIEW B VOLUME 1, NUMBER 7 1 APRIL 1970

Magnetic Phase Diagram of MnF_2 from Ultrasonic and Differential Magnetization Measurements

Y. SHAPIRA AND S. FONER
Francis Bitter National Magnet Laboratory, Massachusetts Institute of Technology, Cambridge, Massachusetts 02139*

(Received 12 December 1969)

The magnetic phase diagram of MnF_2, in the H-T plane, is determined in magnetic fields up to 200 kG directed along the [001] and [100] directions. The magnetic phase transitions appear as anomalies in the ultrasonic attenuation and/or the differential magnetization. Near the various second-order phase transitions, the attenuation of longitudinal sound waves exhibits λ anomalies, whereas near the spin-flop transition (which is a first-order transition) the ultrasonic attenuation exhibits a sharp spike and/or an abrupt increase, depending on the mode of propagation. The spin-flop transition is accompanied by a spike in the differential magnetic moment. The Néel temperature is $T_N=(67.33\pm0.03)$°K, and the triple point for $\mathbf{H}\|[001]$ is at $T_3=(64.9\pm0.1)$°K and $H_3=119\pm2$ kG. The field at the spin-flop transition (for $\mathbf{H}\|[001]$) increases monotonically with temperature from 92 ± 1.5 kG at 4.2°K to 119 ± 2 kG at the triple point. The curvature, at T_N, of the antiferromagnetic-paramagnetic boundary with $\mathbf{H}\|[001]$ is $d^2T/dH^2=-(3.2\pm0.2)\times10^{-10}$ °K/G². The curvature, at T_N, for the antiferromagnetic-paramagnetic boundary with $\mathbf{H}\|[100]$ is smaller by about an order of magnitude. The various phase boundaries are compared with the predictions of the molecular-field theory and other theoretical models.

I. INTRODUCTION

THE magnetic phase diagrams of antiferromagnets have been the subject of theoretical and experimental investigation in the last two decades. The earlier theoretical treatments,[1–4] which were carried out within the framework of the molecular-field approximation, established the general features of such phase diagrams. More recently, phase transitions in antiferromagnets have been treated using more sophisticated theoretical techniques.[5–8]

Experimental work on the phase diagrams of antiferromagnets has been limited by the unavailability of high magnetic fields. Notable exceptions are antiferromagnets with Néel temperatures in the liquid-helium range. Representative examples of work on antiferromagnets with relatively low Néel temperatures can be found in Refs. 9–14. Previous work on the phase diagrams of antiferromagnets with Néel temperatures above $\sim$10°K was largely confined to the spin-flop transition, which was investigated in several materials including MnF_2,[15–17] Cr_2O_3,[18,19] and α-Fe_2O_3.[20,21] However, the antiferromagnetic to paramagnetic transitions in MnF_2 were investigated by Heller in low fields

* Supported by the U. S. Air Force Office of Scientific Research.

[1] C. J. Gorter and T. van Peski-Tinbergen, Physica **22**, 273 (1956).
[2] C. G. B. Garrett, J. Chem. Phys. **19**, 1154 (1951).
[3] T. Nagamiya, K. Yosida, and R. Kubo, Advan. Phys. **4**, 1 (1955). The expression for $B_s'''(0)$ on p. 55 of this reference should be multiplied by 6.
[4] P. Heller, Phys. Rev. **146**, 403 (1966).
[5] H. Falk, Phys. Rev. **133**, A1382 (1964).
[6] F. B. Anderson and H. B. Callen, Phys. Rev. **136**, A1068 (1964).
[7] A. Bienenstock, J. Appl. Phys. **37**, 1459 (1966).
[8] J. Feder and E. Pytte, Phys. Rev. **168**, 640 (1968).
[9] H. M. Gijsman, N. J. Poulis, and J. van den Handel, Physica **25**, 954 (1959).
[10] W. van der Lugt and N. J. Poulis, Physica **26**, 917 (1960).
[11] V. A. Schmidt and S. A. Friedberg, J. Appl. Phys. **38**, 5319 (1967).
[12] J. H. Schelleng and S. A. Friedberg, Phys. Rev. **185**, 728 (1969).
[13] J. E. Rives, Phys. Rev. **162**, 491 (1967).
[14] H. Forstat, P. T. Bailey, and J. R. Ricks, Phys. Letters **30A**, 52 (1969).
[15] I. S. Jacobs, J. Appl. Phys. Suppl. **32**, 61 (1961).
[16] J. de Gunzbourg and J. P. Krebs, J. Phys. (Paris) **29**, 42 (1968).
[17] Y. Shapira and J. Zak, Phys. Rev. **170**, 503 (1968).
[18] S. Foner and S. L. Hou, J. Appl. Phys. Suppl. **33**, 1289 (1962).
[19] Y. Shapira, Phys. Rev. **187**, 734 (1969).
[20] S. Foner and Y. Shapira, Phys. Letters **29A**, 276 (1969).
[21] Y. Shapira, Phys. Rev. **184**, 589 (1969). Earlier work on α-Fe_2O_3 is quoted in this paper.

using NMR,[4] and more recently such transitions were investigated ultrasonically in FeF_2 at high fields.[22] The present work is devoted to the magnetic phase diagram of MnF_2, in fields up to 200 kG. A report on the preliminary results of this work was published earlier.[23]

MnF_2 is ideally suited for a study of the magnetic phase diagram. First, both the crystallographic and the magnetic structures of MnF_2 are comparatively simple. Second, many of the magnetic properties of MnF_2 have been investigated extensively in the past, which facilitates the comparison of new experimental findings with theory. Third, the temperatures between the Néel point and the triple point lie in the liquid-nitrogen range, which is an experimental convenience. Fourth, the magnetic field at the triple point is accessible. Fifth, single crystals of MnF_2 are readily available.

MnF_2 has a rutile structure (tetragonal symmetry) and it is antiferromagnetic below the Néel temperature $T_N = 67.3°K$. In the antiferromagnetic phase there are two interpenetrating sublattices whose magnetizations, at $H=0$, are antiparallel to each other and are directed along the [001] direction (tetragonal axis, or c axis). The anisotropy energy of MnF_2 is uniaxial, with the [001] direction as the preferred axis, and it arises mainly from magnetic dipole-dipole interaction.[24] The exchange energy is much larger than the anisotropy energy and it arises mainly from the antiferromagnetic interaction of each Mn^{++} ion with 8 similar ions on the opposite sublattice. There is also a weak ferromagnetic exchange interaction of each Mn^{++} ion with the two nearest ions on the same sublattice.[25]

Two experimental methods for observing the magnectic phase transitions were used in this work. One method involves the measurement of the differential magnetic moment dM/dH (hereafter DMM) in pulsed magnetic fields. This technique for observing magnetic phase transitions in high fields has been in use for the last decade. The second method involves measurement of the ultrasonic attenuation in steady magnetic fields. The magnetic phase transitions appear as anomalies in the attenuation coefficient. Until recently the study of such anomalies was confined largely to measurements near the Néel temperature of antiferromagnets (Curie temperature of ferromagnets) at zero magnetic field. In particular, the shape of the λ anomaly in the attenuation near T_N was the subject of detailed studies in several materials including MnF_2.[26] More recently, we have shown[22,23] that such λ anomalies also exist near second-order transitions of antiferromagnets in the presence of an applied magnetic field **H**. Different types of anomalies (a sharp spike and/or an abrupt change) in the ultrasonic attenuation occur in antiferromagnets near the spin-flop transition, which is a first-order transition.[17,19,21]

The present work is devoted solely to the determination of the magnetic phase diagram of MnF_2. No attempt is made to explore many other problems which are associated with the magnetic phase transitions. One such problem is the magnetic-field variation of the critical exponent[26,27] in the ultrasonic-attenuation coefficient. Another problem is the exact manner in which the magnetization varies with H, or with T, near the second-order phase transitions.

II. THEORY

As a background for the present experimental study we review some theoretical results concerning the magnetic phase diagram of an antiferromagnet. The discussion is confined to a simple uniaxial antiferromagnet consisting of two identical sublattices, and for which the anisotropy energy is very small compared to the exchange energy. It is assumed that the antiferromagnet is of the easy-axis type, i.e., the sublattice magnetizations at zero applied magnetic field are directed along the axis of symmetry. A direction along the preferred axis will be designated by the unit vector **n**.

The general features of the magnetic phase diagram (in the H-T plane) of an antiferromagnet can be obtained from an analysis based on the molecular-field approximation[1–4] (hereafter MFA). When the external magnetic field **H** is parallel to **n**, the magnetic phase diagram consists of three phases: the paramagnetic (P) phase, the antiferromagnetic (AF) phase, and the spin-flop (SF) phase. In the P phase, the magnetizations $\mathbf{M}_1$ and $\mathbf{M}_2$ of the two sublattices are equal in magnitude and are parallel to each other and to **H**. In the AF phase $\mathbf{M}_1$ and $\mathbf{M}_2$ are parallel (or antiparallel) to **n** but they are either unequal in magnitude and/or are antiparallel to each other. In particular, at $H=0$ the sublattice magnetizations in the AF phase are equal in magnitude but are antiparallel to each other. Finally, in the SF phase $\mathbf{M}_1$ and $\mathbf{M}_2$ make equal but nonzero angles with **H** and are equal in magnitude. If **H** is much smaller than the exchange field H_E then $\mathbf{M}_1$ and $\mathbf{M}_2$ are nearly perpendicular to **H** and are nearly antiparallel to each other. The boundaries between the three phases are sketched in Fig. 1(a). The three phases coexist at the triple point (T_3, H_3).

In the MFA the AF-SF transition is a first-order transition which is accompanied by discontinuous changes in the total magnetization and the magnetic entropy. These predictions are borne out by experi-

[22] Y. Shapira, Phys. Letters **30A**, 388 (1969); and unpublished.
[23] Y. Shapira, S. Foner, and A. Misetich, Phys. Rev. Letters **23**, 98 (1969).
[24] F. Keffer, Phys. Rev. **87**, 608 (1952).
[25] A. Okazaki, K. C. Turberfield, and R. W. H. Stevenson, Phys. Letters **8**, 9 (1964); G. G. Low, A. Okazaki, R. W. H. Stevenson, and K. C. Turberfield, J. Appl. Phys. **35**, 998 (1964).
[26] R. G. Evans, Phys. Letters **27A**, 451 (1968); J. R. Neighbours and R. W. Moss, Phys. Rev. **173**, 542 (1968); A. Ikushima, Phys. Letters **29A**, 364 (1969); B. Lüthi, T. J. Moran, and R. J. Pollina (unpublished).
[27] B. Lüthi and R. J. Pollina, Phys. Rev. **167**, 488 (1968).

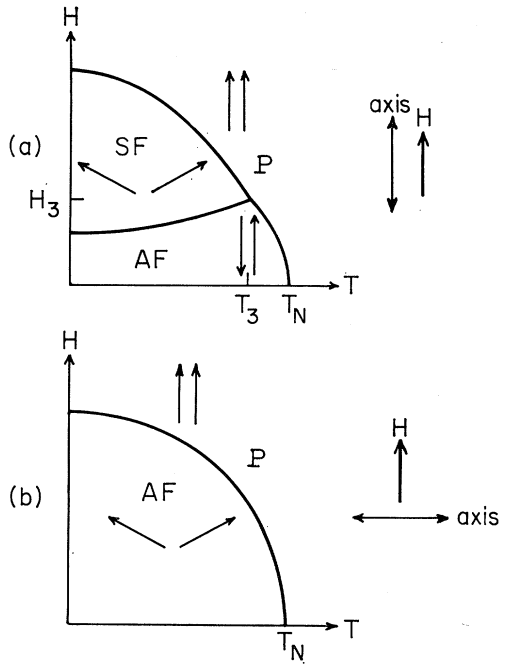

FIG. 1. Schematic phase diagram for a uniaxial antiferromagnet, of the easy-axis type, with weak anisotropy: (a) $\mathbf{H}\|\mathbf{n}$, (b) $\mathbf{H}\perp\mathbf{n}$. The arrows represent the magnetizations of the two sublattices.

ment.[15,16,28] According to the MFA the AF-P and SF-P transitions are second-order transitions in the Ehrenfest sense, i.e., the magnetization and entropy are continuous at the transition, but the differential magnetic moment and the specific heat are discontinuous. It is well known, however, that at T_N the specific heat at $H=0$ exhibits a λ-type anomaly rather than a discontinuity.[29,30] Furthermore, at least in some antiferromagnets, the AF-P transition in a finite magnetic field is also accompanied by a λ-type singularity in the specific heat.[12]

When $\mathbf{H}$ is normal to the preferred axis of the antiferromagnet, the phase diagram consists of only two phases: paramagnetic and antiferromagnetic. In both the P and the AF phases $\mathbf{M}_1$ and $\mathbf{M}_2$ have equal magnitudes. However, in the P phase $\mathbf{M}_1$ and $\mathbf{M}_2$ are both parallel to $\mathbf{H}$, whereas in the AF phase $\mathbf{M}_1$ and $\mathbf{M}_2$ are not parallel to $\mathbf{H}$. The magnetic phase diagram, and the directions of $\mathbf{M}_1$ and $\mathbf{M}_2$, are sketched in Fig. 1(b). In the MFA the AF-P transition is a second-order transition in the Ehrenfest sense. Note that in the AF phase (with $\mathbf{H}\perp\mathbf{n}$) the orientation of $\mathbf{M}_1$ and $\mathbf{M}_2$, relative to each other and relative to $\mathbf{H}$, is similar to the orientation of $\mathbf{M}_1$ and $\mathbf{M}_2$ in the SF phase when $\mathbf{H}\|\mathbf{n}$.

In the following paragraphs we list some formulas for the magnetic phase boundaries.

A. AF-P Transitions

The AF-P boundaries near T_N were calculated in the MFA by Heller.[4] In his calculations it was assumed that the antiferromagnet consisted of two sublattices each of which was coupled to the other by the intersublattice exchange interaction and, in addition, each was coupled internally by the intrasublattice exchange interaction. The external magnetic field $\mathbf{H}$ was assumed to make an arbitrary angle θ with the preferred axis. The AF-P boundary at temperatures just below T_N was found to obey the relation

$$T_N-T=\frac{3(2S^2+2S+1)}{40(S+1)^2}\left[\frac{\chi_N}{M(0,0)}\right]^2 \times T_N H^2(1+2\cos^2\theta), \quad (1)$$

where χ_N is the susceptibility at T_N, $M(0,0)$ is the saturation value of the sublattice magnetization, and S is the spin quantum number.

Let us assume that the exchange interaction arises from the coupling of each spin on sublattice No. 2 to z_1 spins on sublattice No. 1 and to z_2 spins on sublattice No. 2. Further, let the interaction Hamiltonian between two spins, i and j, on opposite sublattices be $-2J_1\mathbf{S}_i\cdot\mathbf{S}_j$, and let the interaction between the two spins on the same sublattice be $-2J_2\mathbf{S}_i\cdot\mathbf{S}_i$. Assuming that $J_1<0$ (antiferromagnetic interaction) and $J_2>0$ (ferromagnetic interaction) one can rewrite Eq. (1) as

$$T_N-T=\frac{g^2\mu_B^2(z_1|J_1|+z_2|J_2|)(2S^2+2S+1)(1+2\cos^2\theta)H^2}{80kz_1^2J_1^2S(S+1)}, \quad (2)$$

where k is the Boltzmann constant, μ_B is the Bohr magneton, and g is the g factor.

In order to bring out the main physical features of the molecular-field calculation we present in the Appendix a calculation for a simplified model in which: (1) the intrasublattice exchange interaction is negligible compared to the intersublattice exchange interaction, (2) the anisotropy energy is very small compared to the exchange energy, and (3) $\mathbf{H}$ is either parallel or perpendicular to $\mathbf{n}$. The first two assumptions are reasonable for MnF_2 because the intrasublattice exchange energy is about 5% of the intersublattice exchange energy, and the anisotropy field is about 1% of the exchange field. The third assumption describes the conditions in the present experiments. Detailed analysis of the model considered in the Appendix was carried out earlier by

[28] In unpublished work by L. J. Neuringer and Y. Shapira, an MnF_2 sample was isolated thermally and a magnetic field $\mathbf{H}$ was applied along the [001] direction. In an increasing magnetic field the temperature of the sample rose at the spin-flop transition, whereas in a decreasing magnetic field the temperature of the sample fell at the transition. These experiments were performed near 4°K.

[29] J. W. Stout and E. Catalano. J. Chem. Phys. **23**, 2013 (1955).

[30] D. T. Teaney, in *Critical Phenomena, Proceedings of a Conference, Washington, D. C., 1965*, edited by M. S. Green and J. V. Sengers, National Bureau of Standards Miscellaneous Publication No. 273 (U. S. Government Printing Office, Washington, D. C., 1966).

Garrett[2] for the special case $S=\frac{1}{2}$. The calculations in the Appendix are for an arbitrary S. These calculations also serve as a convenient starting point for an analysis of the influence of a single-ion anisotropy on the AF-P phase boundaries.[22]

For $\mathbf{H}\perp\mathbf{n}$ this simplified model leads to the following relations for the AF-P boundary near T_N:

$$T_N-T=\frac{g^2\mu_B^2(2S^2+2S+1)H^2}{80kz_1|J_1|S(S+1)} \tag{3}$$

or

$$T_N-T=\frac{g^2\mu_B^2(2S^2+2S+1)H^2}{120k^2T_N}. \tag{4}$$

For $\mathbf{H}\|\mathbf{n}$ the AF-P boundary near T_N satisfies the relation

$$T_N-T=\frac{3g^2\mu_B^2(2S^2+2S+1)H^2}{80kz_1|J_1|S(S+1)} \tag{5}$$

or

$$T_N-T=\frac{g^2\mu_B^2(2S^2+2S+1)H^2}{40k^2T_N}. \tag{6}$$

Equations (3) and (5) are easily obtained from Eq. (2) by setting $J_2=0$.

It is interesting to note that for a given spin quantum number S Eqs. (4) and (6) have the form of a "law of corresponding states." Defining a reduced temperature $t=T/T_N$ and a reduced field

$$h=g\mu_B[S(S+1)]^{1/2}H/kT_N, \tag{7}$$

we can write Eq. (6), for example, in the form

$$t=1-ah^2, \tag{8}$$

where

$$a=(2S^2+2S+1)/40S(S+1). \tag{9}$$

In casting Eq. (1) into the form of Eq. (2), we used certain relations between χ_N, T_N, and J_1 and J_2 which are valid only in the MFA. Thus, while Eqs. (1) and (2) are equivalent *in the MFA*, they may lead to somewhat different numerical results when *experimental values* for χ_N, T_N, J_1, and J_2 are used, because these experimental values are not interrelated according to the MFA. A similar remark applies to the equivalence of Eqs. (3) and (4) and of Eqs. (5) and (6).

The discussion thus far was based on the MFA. A more general thermodynamic relation for the AF-P boundary near T_N, with $\mathbf{H}\|\mathbf{n}$, was given by Skalyo *et al.*[31] This relation is based on a result, derived earlier by Fisher,[32] for a simple (two sublattice) uniaxial antiferromagnet (of the easy-axis type) in which the only magnetic interaction is the intersublattice exchange interaction. These assumptions are reasonable for MnF_2. Based on his model Fisher showed that the magnetic contribution to the specific heat C_m (at $H=0$) is related to the low-field susceptibility χ_{II} (for $\mathbf{H}\|\mathbf{n}$) by the equation

$$C_m=A\,\partial[T\chi_{II}(T)]/\partial T, \tag{10}$$

where A is a slowly varying function of T near T_N. At T_N the coefficient A can be estimated from the relation

$$A=3z_1|J_1|kf[1-(\tfrac{2}{3}\gamma)]/g^2\mu_B^2, \tag{11}$$

where f is a factor of order unity, and $\gamma=0$ for an isotropic Heisenberg interaction. Using a thermodynamic argument, Skalyo *et al.* have shown that at T_N the AF-P boundary for $\mathbf{H}\|\mathbf{n}$ obeys the relation

$$d^2T/dH^2=-A^{-1}. \tag{12}$$

Assuming the form

$$T_N-T=DH^2 \tag{13}$$

for the AF-P boundary near T_N one obtains

$$D=1/(2A). \tag{14}$$

Numerical calculations for the AF-P transition in an Ising antiferromagnet with $\mathbf{H}$ along $\mathbf{n}$ were carried out by Bienenstock.[7] Assuming two interpenetrating sublattices and $J_2=0$ the AF-P boundary was found to be well described by the equation

$$T=T_N[1-(H/H_c)^2]^{\xi}, \tag{15}$$

where $H_c=2Sz_1|J_1|/g\mu_B$, and $\xi=0.87$, 0.35, and 0.36 for a square, a simple cubic, and a bcc lattice, respectively.

B. SF-P Transition

Consider the SF phase when $\mathbf{H}\|\mathbf{n}$. As mentioned earlier, the orientation of $\mathbf{M}_1$ and $\mathbf{M}_2$, relative to each other and relative to $\mathbf{H}$, is similar to the orientation of $\mathbf{M}_1$ and $\mathbf{M}_2$ in the AF phase when $\mathbf{H}\perp\mathbf{n}$. The difference between the two cases arises from the anisotropy interaction. Assuming again that the anisotropy interaction is small compared to the exchange interaction, the MFA leads to a SF-P phase boundary (for $\mathbf{H}\|\mathbf{n}$) which is nearly the same as the AF-P boundary with $\mathbf{H}\perp\mathbf{n}$.[3] The main difference is that when the SF-P boundary is extrapolated to fields below H_3, it intersects the T axis at a temperature T_N^* which is slightly lower than T_N. At temperatures near T_N^*, the SF-P boundary is given approximately by Eq. (2) with $\theta=90°$ [which reduces to Eqs. (3) or (4) if $|J_2|\ll|J_1|$], except that T_N is replaced by T_N^*. For more sophisticated treatments of the SF-P phase boundary see Refs. 5, 6, and 8.

C. AF-SF Transition

The AF-SF transition, with $\mathbf{H}\|\mathbf{n}$ and at $T<T_3$, has been discussed extensively in the literature.[3,33] This transition is often referred to as the spin-flop transition.

[31] J. Skalyo, Jr., A. F. Cohen, S. A. Friedberg, and R. B. Griffiths, Phys. Rev. **164**, 705 (1967).
[32] M. E. Fisher, Phil. Mag. **7**, 1731 (1962).
[33] J. Kanamori in *Magnetism*, edited by G. T. Rado and H. Suhl (Academic Press, Inc., New York, 1963), Vol. I, p. 127.

A standard formula for the spin-flop transition field H_{SF} is

$$H_{SF}=[2K/(\chi_\perp-\chi_{||})]^{1/2}, \tag{16}$$

where K is the anisotropy energy per unit volume, and $\chi_{||}$ and $\chi_\perp$ are the (low-field) susceptibilities per unit volume for $\mathbf{H}$ parallel and perpendicular to $\mathbf{n}$, respectively. In order to expose the limitations of Eq. (16) we present a derivation of this equation.

The equilibrium configuration of the sublattice magnetizations $\mathbf{M}_1$ and $\mathbf{M}_2$ at a given temperature T, magnetic field H, and pressure P, is that configuration which has the lowest value for the thermodynamic potential $\Phi(T,P,H)$. The thermodynamic potential Φ plays a role similar to that which the Gibbs free energy $G(T,P)$ plays for a simple nonmagnetic system. Consider first the equilibrium configuration at $H=0$, i.e., the configuration in the AF phase with $\mathbf{M}_1$ and $\mathbf{M}_2$ pointing along $\pm\mathbf{n}$. In this configuration $\mathbf{L}=\mathbf{M}_1-\mathbf{M}_2$ is parallel to $\mathbf{n}$. Next consider a second configuration at $H=0$ (not the equilibrium configuration) in which: (a) $\mathbf{L}$ is perpendicular to $\mathbf{n}$, and (b) the thermodynamic potential Φ is minimum relative to all configurations with $\mathbf{L}\perp\mathbf{n}$. Physically, the condition $\mathbf{L}\perp\mathbf{n}$ implies that the component of $\mathbf{M}_1$ along $\mathbf{n}$ is equal both in magnitude *and in sign* to the component of $\mathbf{M}_2$ along $\mathbf{n}$. The antiferromagnetic exchange interaction tends, in this case, to align $\mathbf{M}_1$ and $\mathbf{M}_2$ normal to $\mathbf{n}$. One then expects that in the configuration which minimizes Φ under the restriction $\mathbf{L}\perp\mathbf{n}$ (for weak anisotropy and at $H=0$), $\mathbf{M}_1$ and $\mathbf{M}_2$ are perpendicular to $\mathbf{n}$, are equal in magnitude, and are antiparallel to each other. At $H=0$ the thermodynamic potential of this configuration should be higher by $\Delta\Phi$ than the thermodynamic potential Φ_{AF} in the AF phase. We call $\Delta\Phi$ the anisotropy energy K.

The change of $\Phi(T,P,H)$ in a given phase can be obtained by integrating the differential

$$d\Phi=-SdT+VdP-MdH, \tag{17}$$

where S, V, and M are the entropy, volume, and magnetization in that phase, respectively. Assuming that T and P are fixed, and taking $\Phi=0$ for the AF phase at $H=0$, one has

$$\Phi_{AF}(H)=-\int_0^H M(H')dH'. \tag{18}$$

For $\mathbf{H}\|\mathbf{n}$ and assuming that $\chi_{||}$ is independent of H, one obtains

$$\Phi_{AF}(H)=-(\tfrac{1}{2}\chi_{||}H^2). \tag{19}$$

Now consider the configuration which minimizes Φ under the restriction $\mathbf{L}\perp\mathbf{n}$. At $H>H_{SF}$ this configuration is the equilibrium configuration (in the SF phase), whereas at $H<H_{SF}$ it is a nonequilibrium configuration. We designate the thermodynamic potential of this configuration (at all fields) by Φ_{SF} and the susceptibility of this configuration by χ_{SF}. Then

$$\Phi_{SF}(H)=K-\int_0^H M(H')dH'. \tag{20}$$

Assuming that χ_{SF} is field-independent one has

$$\Phi_{SF}(H)=K-(\tfrac{1}{2}\chi_{SF}H^2). \tag{21}$$

When the anisotropy energy is very small compared to the exchange energy, χ_{SF} is very nearly equal to $\chi_\perp$. In this case

$$\Phi_{SF}(H)=K-(\tfrac{1}{2}\chi_\perp H^2). \tag{22}$$

In general, $\chi_\perp>\chi_{||}$ for $T<T_N$. Therefore Φ_{SF} decreases faster with H than Φ_{AF}. Thus, while Φ_{SF} is higher than Φ_{AF} at $H=0$, it becomes lower than Φ_{AF} at sufficiently high fields. The transition field H_{SF} is obtained by equating the right sides of Eqs. (19) and (22), which leads to Eq. (16).

The most serious shortcoming of the above derivation, in the case of a uniaxial antiferromagnet with very low anisotropy, is the assumption that $\chi_{||}$ is field-independent. Using the MFA one can show that while $\chi_\perp$ is field-independent, $\chi_{||}$ tends to increase with H. As a result, the spin-flop transition occurs at a higher magnetic field than is calculated from Eq. (16) using the low-field values of $\chi_{||}$ and $\chi_\perp$. The effect of the field dependence of $\chi_{||}$ on H_{SF} is small, however, except at temperatures close to T_3 (see Sec. V and note added in proof).

It is possible to relate H_{SF} to the antiferromagnetic-resonance frequency ω_0 at $H=0$. According to Kanamori and Tachiki[34]

$$\omega_0=\gamma(2K/\chi_\perp)^{1/2}, \tag{23}$$

where $\gamma=g\mu_B/\hbar$ is the gyromagnetic ratio. Combining Eqs. (16) and (23) one obtains

$$H_{SF}=\omega_0/\gamma(1-\alpha)^{1/2}, \tag{24}$$

where $\alpha=\chi_{||}/\chi_\perp$. Since Eq. (24) is based on Eq. (16), it suffers from the same limitations.

III. EXPERIMENTAL PROCEDURE

The experimental results reported below were obtained on the same single crystal of MnF_2 which had been used in the earlier work on the spin-flop transition at 4.2°K.[17] Semiquantitative spectroscopic analysis performed on a part of this crystal gave the following concentrations, in ppm (by weight), for the principal impurities: Al, from 10 to 100; Ca, from 10 to 100; Mg, from 10 to 100; Si, from 10 to 100; Cu, ~10; Fe, ~10; Ge, ~10; Sn, ~10; Cr, from 1 to 10. Some preliminary data, less accurate than (but consistent with) those

[34] J. Kanamori and M. Tachiki, J. Phys. Soc. Japan 17, 1384 (1962).

presented below, were taken on a second single crystal which was obtained from Optovac.[35]

Two types of experiments were performed: differential magnetization in pulsed magnetic fields, and ultrasonic attenuation in steady magnetic fields. The experimental techniques used in these two types of measurements were completely different. The ultrasonic measurements are discussed first.

A. Ultrasonic Measurements

The attenuation of 10 to 50 MHz longitudinal and shear ultrasonic waves was measured using pulse techniques. The longitudinal and shear waves were generated by X-cut and Y-cut quartz transducers, respectively. The transducers were bonded to the sample using Dow Corning 200 silicone fluid having a viscosity of 30 000 cS at 25°C. The attenuation was measured by gating one of the acoustical echoes, integrating it, and recording the output as a function of either T or H. This technique is very convenient and accurate for determining the position (in the H-T plane) of a phase transition, but is not always the most accurate method for determining the detailed line shape of the anomaly observed near the phase transition. In general, the attenuation was measured either as a function of T at constant H, or as a function of H at constant T.

The original sample used in the ultrasonic experiments was approximately cubic with an edge of $\sim$6 mm. The faces of this sample, which were normal to the [100], [010], and [001] directions, were lapped for ultrasonic work. After taking all the data for acoustical modes with propagation vector $\mathbf{q}$ along the [100] direction, the sample was cut to obtain two parallel [110] faces separated by $\sim$4 mm. Data for longitudinal waves with $\mathbf{q}\|[110]$ were then taken. The attenuation of sound waves with $\mathbf{q}\|[001]$ was investigated before and after the sample was cut.

Most of the ultrasonic data were taken at $63 \lesssim T < 78$°K with the sample immersed in liquid nitrogen. The temperature was measured with a calibrated platinum resistance thermometer, obtained from Rosemount Engineering Co.,[36] which was placed near the sample. To obtain higher accuracy, the calibration of this platinum thermometer was checked at 77.6°K and at 67.3°K against another Rosemount platinum thermometer which had been calibrated by the National Bureau of Standards. The two calibrations differed by 0.05°K at 77.6°K, and by 0.04°K at 67.3°K. The temperatures given below were adjusted so as to agree with the NBS calibration in which the NBS 1955 temperature scale was used.

One difficulty encountered in measuring temperatures in high magnetic fields was the magnetoresistance of the platinum resistance thermometer. This magnetoresistance depends on T, and on both the magnitude of the field $\mathbf{H}$ and its orientation relative to the thermometer. To obtain the correct temperature, the magnetoresistance must be subtracted from the measured resistance. The magnetoresistance itself was measured by immersing the platinum thermometer in liquid nitrogen, maintaining a constant temperature by keeping the vapor pressure over the nitrogen bath constant, and measuring the resistance of the thermometer as a function of H. At 65°K and with a field of 200 kG directed along the long axis of the thermometer, the magnetoresistance was equivalent to a temperature change of 2.5°K. The resistance $R(H)$ was measured to an accuracy of 0.1%, which is equivalent to a temperature change of 0.04°K. Our results for the magnetoresistance at 65°K are in excellent agreement with independent measurements by Neuringer *et al.* who used a different technique which involved gas thermometry.[37] The estimated accuracy of the temperature measurements in the ultrasonic experiments is 0.03°K at $H=0$, and 0.06°K at high magnetic fields.

Steady magnetic fields were produced by Bitter-type solenoids. Most of these solenoids were capable of producing fields up to 150 kG in a 54-mm bore. One solenoid produced fields up to 200 kG in a 32-mm bore. The magnetic field was known to an accuracy of $\sim$0.5%.

B. DMM Measurements

DMM measurements were carried out in pulsed fields generated in multilayer copper coils, which were immersed in liquid nitrogen for efficient field generation. Reproducible fields with a half-period of 10 msec were generated in a 2-cm-i.d. coil using a 0.0125-F, 100-kJ capacitor bank. The large i.d. permitted insertion of a conventional glass Dewar which contained the pickup coil assembly, sample, thermometer, and supporting structure. Fields up to 450 kG could be generated. The accuracy of the field measurements was $\pm$1% for all the experimental results reported here.

The DMM measurements were made with an arrangement similar to that discussed earlier.[18] Improved sensitivity was achieved by using two coaxial, series-opposing, pickup coils which had a common center. The area turns of these two coils were balanced to 1%. The residual background signal, during the pulse and with the sample in place, was reduced by bucking it out using a portion of the *emf* generated in a third coaxial pickup coil. With this technique any signal which was both in phase with and proportional to the time rate of change of the applied field, was balanced to 0.1%. When the temperature was varied over a large interval, it was sometimes necessary to readjust the balance. These refinements, additional filtering, and the rather long pulse resulted in a sensitivity which was about 100 times higher than that of the earlier system.[18]

Some runs were performed over the range $4.2\text{°K} < T$

[35] Optovac, Inc., North Brookfield, Mass.
[36] Rosemount Engineering Co., Minneapolis, Minn.
[37] L. J. Neuringer, A. Perlman, L. G. Rubin, and Y. Shapira (unpublished).

$<T_N$ while others were limited to the interval $64°K \lesssim T < T_N$. To cover the range 4.2°K to T_N, the sample was placed in a Dewar which was filled with liquid helium. As the level of the liquid helium dropped below the position of the sample, the temperature of the sample started to rise slowly (about 2 h from 4.2 to 77°K). Data were taken as the sample warmed up gradually. Runs in the interval $64°K \lesssim T < T_N$ were carried out by placing the sample in a liquid-nitrogen bath and regulating the vapor pressure over the bath. In all runs, the temperature was measured with a Cu-constantan thermocouple which was in contact with the sample. The accuracy of the temperature measurements was better than 2°K. In those runs where the sample was in liquid nitrogen, the differential accuracy was 0.1°K.

One difficulty with the thermometry in the pulsed-field experiments arises from the fact that the temperature is measured at zero field before and after the pulse, but not during the pulse. During the pulse the sample may not be in thermal equilibrium with its surrounding (e.g., the nitrogen bath) because the thermal relaxation time may not be short compared to the duration of the pulse. Thus the temperature measured at $H=0$ may not be exactly the same as the temperature at the instant when the phase transition occurs. Estimates show that this error may become significant when the transition field varies strongly with temperature, e.g., the AF-P boundaries near T_N. For the AF-SF transition we expect that this error in the temperature does not affect our results significantly.

Samples for the DMM measurements were cut from the same single crystal which was used for the ultrasonic measurements. These samples were right circular cylinders with diameters and lengths from 1 to 2 mm. The length-to-diameter ratio varied from 1 to 2. The axis of each cylinder was parallel, within about 2°, to either the [100] of the [001] direction.

Demagnetizing effects were small. The largest value of $4\pi\chi$ in MnF_2 is about 1.3×10^{-2} so that the largest possible demagnetizing field is 1.3% of the applied field. The actual demagnetizing field in the present experiments was estimated to be less than 1% of the external field. No corrections for these effects were made in either the DMM measurements or the ultrasonic measurements.

IV. EXPERIMENTAL RESULTS

The experimental results near each phase-boundary line are presented separately. We start with the determination of the Néel temperature and then present the data for transitions in fields parallel and perpendicular to the [001] direction, which is the preferred axis.

A. Néel Temperature

The attenuation of 10- to 50-MHz longitudinal ultrasonic waves propagating along the [100], [110], and [001] directions was measured at $H=0$ as a function of temperature. A λ-type anomaly in the attenuation, similar to the one reported earlier by other workers,[26] was observed near the Néel temperature. For a 30-MHz longitudinal wave with a propagation vector $\mathbf{q}$, the magnitude of the attenuation anomaly was ~3 dB/cm for $\mathbf{q}\|[100]$, ~1.5 dB/cm for $\mathbf{q}\|[110]$, and ~5 dB/cm for $\mathbf{q}\|[001]$. The temparature of the attenuation maximum did not change by more than 0.03°K as the ultrasonic frequency was varied from 10 to 50 MHz. The Néel temperature, determined from the position of the attenuation maximum, is $T_N=(67.33\pm0.03)$°K, in very good agreement with the value given by Heller.[4]

Experiments were made with 30-MHz shear waves propagating along the [001] direction. No anomaly was observed near T_N, to within the experimental resolution of 0.04 dB/cm. A similar result was obtained by Evans and by Neighbours and Moss.[26]

B. H‖[001]

Results for the three phase boundaries: AF-P, SF-P, and AF-SF are discussed separately.

1. AF–P Transition

The attenuation of longitudinal ultrasonic waves propagating along the [100], [110], and [001] directions exhibits a λ-type anomaly at the AF-P boundary in finite magnetic fields. This anomaly was observed by measuring the attenuation either as a function of H at constant T, or as a function of T at constant H. Figure 2 shows a trace of the λ-anomaly in the attenuation at the AF-P boundary. The maximum value of the attenuation in this trace is ~5 dB/cm above the value at the highest fields. In the H-T plane, the position of the attenuation maximum was independent (within experimental accuracy) of both the direction of propagation of the longitudinal wave and its frequency. The AF-P boundary obtained from these measurements is shown in Fig. 3. Most of these data were obtained by measuring the attenuation of 30-MHz longitudinal ultrasonic waves, with $\mathbf{q}\|[001]$, as a function of T at constant H.

For a given longitudinal mode of propagation and frequency, the magnitude of the attenuation anomaly was roughly the same along the entire AF-P boundary. We also performed experiments with 30-MHz *shear* waves propagating along the [001] direction. Near the AF-P boundary at 76 kG, no anomaly in the attenuation was found to within the experimental resolution of 0.04 dB/cm.

A plot of $\log(T_N-T)$ versus $\log H$ for the AF-P boundary with $\mathbf{H}\|[001]$ showed that $T_N-T\cong DH^n$, where D is a constant and $n\cong2.0$. A plot of T_N-T versus H^2 is shown in Fig. 4. The data for the AF-P boundary were fitted to the equations

$$T=T_N-D_1H^2, \tag{25a}$$

$$T=T_N-D_1H^2-D_2H^4, \tag{25b}$$

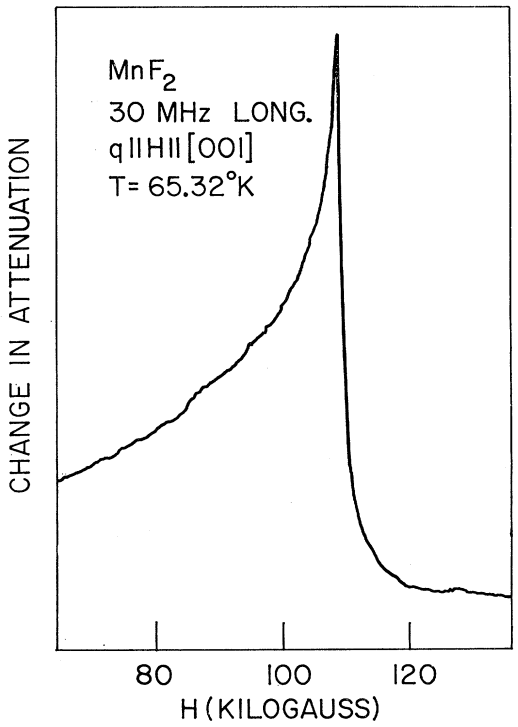

FIG. 2. Recorder tracing of the attenuation of 30-MHz longitudinal ultrasonic waves near the AF-P boundary with $\mathbf{H}\|[001]$. The trace was obtained by maintaining T at 65.32°K and varying H.

and

$$T=T_N-D_1H^2-D_2H^4-D_3H^6, \qquad (25c)$$

using the least-squares method and treating T_N and D_i as adjustable parameters. For Eq. (25a) we obtained $T_N=(67.346\pm0.005)$°K and $D_1=(1.690\pm0.006)\times10^{-10}$ °K/G², with an rms residual of 0.032°K. A similar fit by Heller[4] to his low-field results gave $D_1=(1.95\pm0.3)\times10^{-10}$ °K/G². For Eq. (25b) we obtained $T_N=(67.324\pm0.003)$°K, $D_1=(1.508\pm0.014)\times10^{-10}$ °K/G², and $D_2=(1.485\pm0.11)\times10^{-21}$ °K/G⁴, with an rms residual of 0.020°K. For Eq. (25c) we obtained $T_N=(67.327\pm0.004)$°K,

$$D_1=(1.588\pm0.033)\times10^{-10}\ \text{°K/G}^2,$$
$$D_2=-(2.43\pm6.6)\times10^{-22}\ \text{°K/G}^4,$$

and

$$D_3=(8.95\pm3.4)\times10^{-32}\ \text{°K/G}^6,$$

with an rms residue of 0.019°K. The best fits to Eqs. (25a) and (25b) are shown in Fig. 4 as a solid line and as a broken line, respectively. From the results above we estimated that

$$(d^2T/dH^2)_{T_N}=-(3.2\pm0.2)\times10^{-10}\ \text{°K/G}^2.$$

Note that the values of T_N obtained from these fits are in excellent agreement with the value $T_N=(67.33\pm0.03)$°K obtained from the zero-field data.

The AF-P transition was also observed in the DMM measurements which were carried out in pulsed fields. At temperatures near T_N the DMM had a step at the

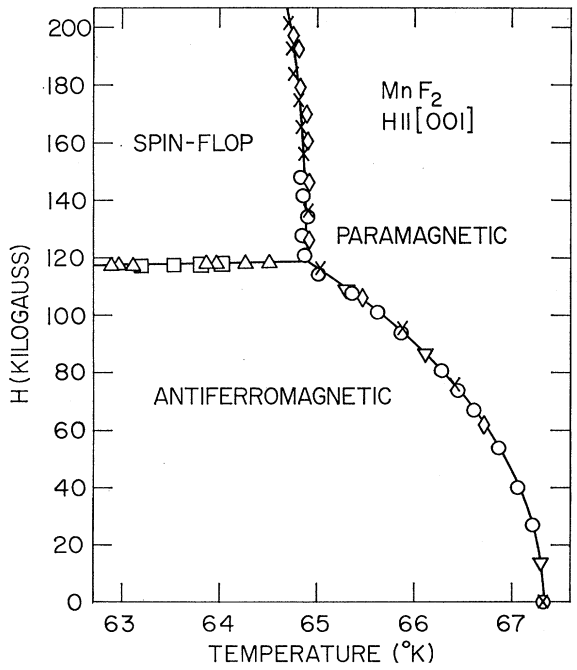

FIG. 3. Magnetic phase diagram at $63\lesssim T<67.5$°K and with $\mathbf{H}\|[001]$. The data points were obtained from ultrasonic attenuation measurements.

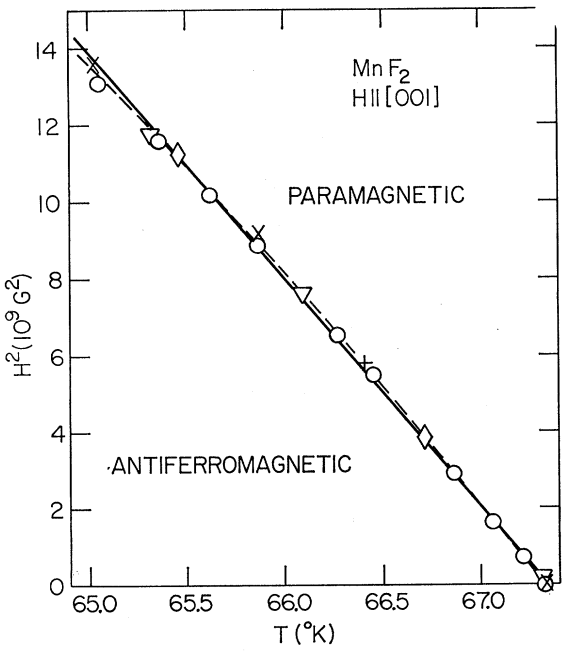

FIG. 4. A plot of H^2 versus T for the AF-P boundary with $\mathbf{H}\|[001]$. The data points are from ultrasonic attenuation measurements. The solid and broken lines represent best fits to Eqs. (25a) and (25b), respectively.

transition. As T approached T_3, however, the character of the transition changed smoothly from a step to a spike. The AF-P boundary obtained from the DMM measurements was in agreement with the ultrasonic data.[23] However, as mentioned in Sec. III, the DMM data may contain errors in the temperature since the temperature, which is measured only at $H=0$, may vary during the pulse. For this reason we shall not present the DMM data here.

2. SF–P Transition

The ultrasonic measurements near the SF-P boundary were carried out with 10- and 30-MHz longitudinal waves propagating along the [001] direction. With $\mathbf{H}\|[001]$, the attenuation, measured as a function of T at constant H, exhibited a λ-type anomaly. Figure 5 shows a recorder tracing of this anomaly at $H=133.4$ kG. The magnitude of the anomaly in this trace is ~ 4 dB/cm.

The SF-P boundary deduced from the ultrasonic data is shown in Fig. 3. Because the boundary line is very steep, it is difficult to ascertain whether T varies linearly with H^2. If one assumes that $T=-DH^2+\text{const}$ then $D=(7\pm 3)\times 10^{-12}$ °K/G^2.

The SF-P boundary was not detected in the DMM measurements with fields up to 220 kG. One possible reason is that the boundary line is very steep. For such a boundary it is easier to observe a transition by varying T at constant H rather than to observe it by fixing T and varying H.

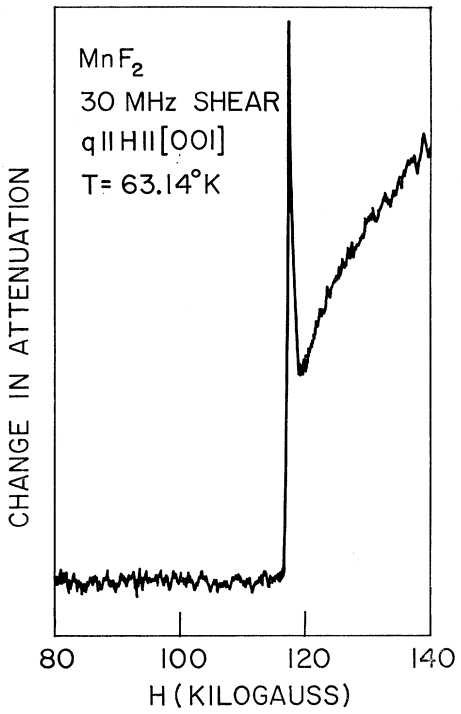

FIG. 6. Recorder tracing of the attenuation of 30-MHz shear ultrasonic waves (with $\mathbf{q}\|[001]$) near the spin-flop transition with $\mathbf{H}\|[001]$. The trace was obtained by maintaining T at 63.14°K and varying H.

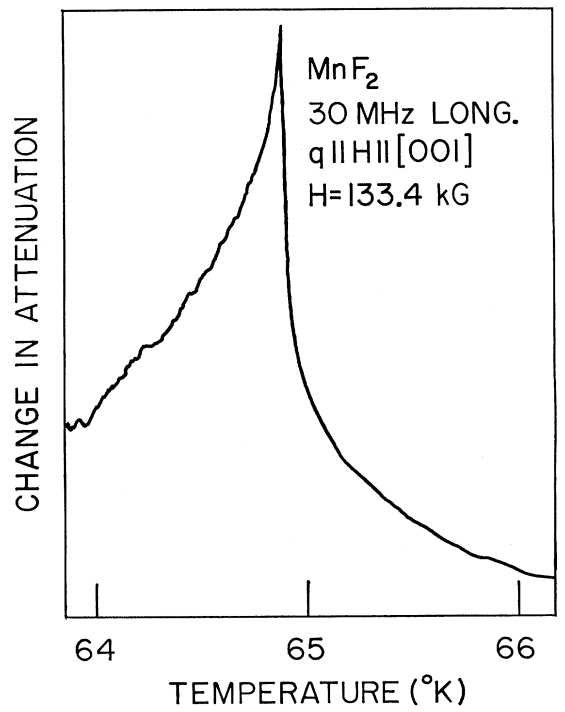

FIG. 5. Recorder tracing of the attenuation of 30-MHz longitudinal ultrasonic waves near the SF-P boundary with $\mathbf{H}\|[001]$. The trace was obtained by keeping H at 133.4 kG and varying T.

3. AF–SF Transition (Spin-Flop)

The spin-flop transition was previously studied ultrasonically at 4.2°K and the results have been discussed in detail.[17] It was found that for several modes of propagation either a sharp spike in the attenuation occurs at the spin-flop transition and/or the attenuation increases abruptly at the transition. These phenomena were observed only when $\mathbf{H}$ was aligned very accurately along the [001] direction. The spin-flop transition was also observed ultrasonically at 20.3°K.[23]

In the present work the spin-flop transition was investigated ultrasonically at $63°\text{K}\lesssim T<T_3$. Two modes of propagation were studied: longitudinal waves with $\mathbf{q}\|[100]$, and shear waves with $\mathbf{q}\|[001]$. The attenuation of either mode was measured as a function of H at constant T. With $\mathbf{H}$ accurately aligned along the [001] direction, the attenuation of the longitudinal mode increased abruptly (like a step function) at the spin-flop transition. In an increasing H, the attenuation of the shear mode exhibited a sharp spike at the transition and then remained higher at $H>H_{SF}$ than at $H<H_{SF}$. Figure 6 illustrates some of the results obtained with the shear mode. The magnitude of the spike in this figure was ~ 0.5 dB/cm. The spike decreased in

magnitude as T increased toward T_3. The AF-SF boundary obtained from the ultrasonic measurements at $63°K \lesssim T < T_3$ is shown in Fig. 3.

The spin-flop transition was observed in the DMM measurements in pulsed magnetic fields. A sharp spike ($\sim$2.5 kG wide at 4.2°K, and $\sim$3.5 kG wide at 64°K) in the DMM marked the transition. At 4.2°K the DMM measurements gave $H_{SF}=91\pm1$ kG as compared to $H_{SF}=92.4\pm0.5$ kG obtained from the ultrasonic data. At the triple point the DMM results gave $H_3=119\pm2$ kG, in agreement with the ultrasonic data. The temperature variation of H_{SF} is shown in Fig. 7.

4. *Triple Point*

The triple point (T_3, H_3) is obtained from the intersection of the three boundary lines: AF-P, AF-SF, SF-P. Our data give $T_3=(64.9\pm0.1)°K$, $H_3=119\pm2$ kG.

C. H‖[100]

Ultrasonic measurements with **H**‖[100] were carried out using 10- and 30-MHz longitudinal waves propagating along either the [100] or the [001] direction. A λ-type anomaly in the attenuation was observed at the AF-P transition. The position (in the H-T plane) of the attenuation maximum was independent of the frequency and direction of propagation of the sound wave, within the experimental accuracy. For a given mode of propagation and frequency, the magnitude of the λ anomaly was roughly the same along the entire AF-P boundary. The AF-P boundary obtained from the ultrasonic measurements is shown in Fig. 8. Most of these data were obtained by studying the attenuation of 30-MHz longitudinal waves with **q**‖**H**‖[100] as a function of T at constant H.

A plot of $\log(T_N-T)$ versus $\log H$ for the AF-P boundary showed that $T_N-T\cong DH^2$, where D is a constant and $n\approx2$. The data for the AF-P boundary were also fitted to Eqs. (25a) and (25b). The best fit to Eq. (25a), shown as a solid line in Fig. 8, gave $T_N=(67.346\pm0.003)°K$ and $D_1=(1.63\pm0.01)\times10^{-11}\,°K/G^2$, with an rms residual of 0.026°K. The best fit to Eq. (25b), shown as a broken line in Fig. 8, gave $T_N=(67.333\pm0.003)°K$, $D_1=(1.31\pm0.04)\times10^{-11}\,°K/G^2$, and $D_2=(8.9\pm1.1)\times10^{-23}\,°K/G^4$, with an rms residual of 0.023°K. The above values for D_1 are substantially lower than the value $(7.5\pm3)\times10^{-11}\,°K/G^2$ obtained by Heller[4] from his low-field results.

Attempts to observe the AF-P transition, for **H**‖[100], by DMM measurements in pulsed fields up to 220 kG were unsuccessful. As in the case of the SF-P transition with **H**‖[001], the difficulty may be related to the very rapid variation of the transition field with T.

V. DISCUSSION

Previous experiments have shown that when $H=0$ a λ anomaly in the attenuation of longitudinal sound waves occurs at T_N. The present experiments demonstrate that such λ anomalies also occur at the AF-P transitions with both **H**‖**n** and **H**⊥**n**, as well as at the SF-P transition. Thus, λ anomalies in the attenuation of longitudinal sound waves occur near all the transi-

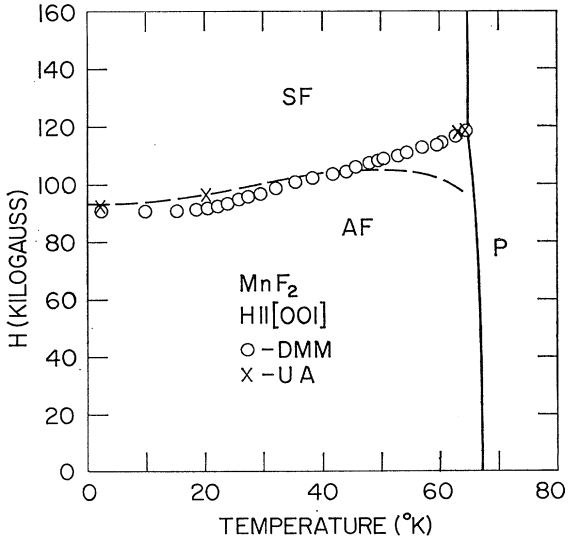

FIG. 7. AF-SF phase boundary (with **H**‖[001]) as determined from DMM and ultrasonic attenuation (UA) measurements. The broken line was calculated from Eq. (24) using data of Refs. 38, 39, and 41. The limitations of Eq. (24) at temperatures near T_3 are discussed in the text.

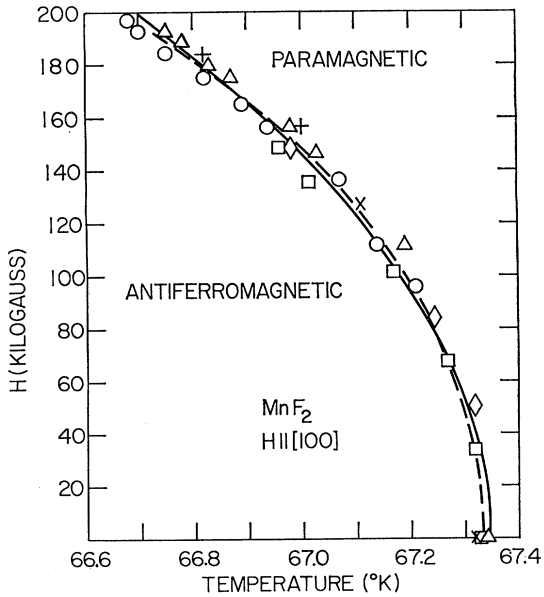

FIG. 8. Magnetic phase diagram near T_N and with **H**‖[100]. The data points are from ultrasonic-attenuation measurements. The solid and broken lines represent best fits to Eqs. (25a) and (25b), respectively.

tions which according to the MFA are second-order transitions.

In MnF_2 the magnetic interaction is predominantly an isotropic exchange interaction. The spin-phonon coupling mechanism in this case is expected to be the volume magnetostrictive coupling which does not lead to λ anomalies in the attenuation of shear waves propagating along a symmetry direction.[27] The data for shear waves, obtained near T_N (at $H=0$) and near the AF-P transition with $\mathbf{H}\|[001]$, are consistent with this prediction.

The physical mechanisms which may lead to the observed ultrasonic behavior near the AF-SF transition (spin-flop transition) were discussed in Refs. 17, 19, and 21. The most likely explanation of this behavior is based on the interaction of sound waves with antiferromagnetic domains. The fact that the attenuation peak (spike) at H_{SF} is very sharp even at temperatures close to T_3 (see Fig. 6) is consistent with this explanation. An alternative explanation of the spike is based on a phonon-magnon resonance. However, the magnon lifetime at temperatures near T_3 is very short,[38] so that the observed width of the spike at H_{SF} is much narrower than that expected for a phonon-magnon resonance.

The sharp spike *in the DMM* at the spin-flop transition indicates an abrupt magnetization change. This agrees with the theoretical prediction (Sec. II) and with earlier observations.[15,16]

The *qualitative* features of the magnetic phase diagram of MnF_2 are correctly predicted by the MFA. As we shall see, however, the MFA leads to incorrect *quantitative* predictions. Consider first the AF-P boundary with $\mathbf{H}\|[001]$. According to the MFA, at temperatures just below T_N this phase boundary should obey Eq. (25a) with $D_1=$ const, as is observed. The value for D_1 given by the MFA is: $D_1=0.7\times10^{-10}$ °K/G² from Eq. (1), and the susceptibility data of Trapp[39]; $D_1=1.06\times10^{-10}$ °K/G² from Eq. (2) using the neutron diffraction results of Okazaki *et al.*[25] ($J_1/k=-1.76$°K, $J_2/k=0.32$°K) and the values $S=\frac{5}{2}$, $z_1=8$, $z_2=2$; $D_1=1.02\times10^{-10}$ °K/G² from Eq. (5); and $D_1=1.24\times10^{-10}$ °K/G² from Eq. (6). All these values for D_1 are lower than the experimental value $D_1=(1.6\pm0.1)\times10^{-10}$ °K/G² obtained from fits to Eqs. (25).

To compare the experimental results with Bienenstock's calculations for an Ising antiferromagnet, we expanded the right side of Eq. (15) letting $\xi=0.36$. This gave $D_1=0.88\times10^{-10}$ °K/G², which is much lower than the experimental value.

The curvature of the AF-P boundary with $\mathbf{H}\|[001]$ is related in Eq. (12) to the coefficient A. To test this equation one needs the value of A at T_N. This value is obtained by analyzing specific-heat data together with susceptibility data using Eq. (10). The specific heat of MnF_2 was measured by Stout and Catalano,[29] and more recently by Teaney.[30] The susceptibility was measured by Foner[40] and by Trapp.[39] To obtain A (at T_N) we analyzed all four combinations of specific-heat and susceptibility data. The four values for A were approximately the same, ranging from $(3.0\pm0.3)\times10^9$ G²/°K to $(3.2\pm0.2)\times10^9$ G²/°K. Using Eq. (12) these two extreme values for A lead to $d^2T/dH^2=-(3.3\pm0.3)\times10^{-10}$ °K/G² and $d^2T/dH^2=-(3.1\pm0.2)\times10^{-10}$ °K/G² for the AF-P phase boundary at T_N. The experimental value $d^2T/dH^2=-(3.2\pm0.2)\times10^{-10}$ °K/G² at T_N is in very good agreement with these predictions.

It is also interesting to compare the experimental value of A at T_N with Fisher's theoretical estimate, which is given by Eq. (11). Setting $f=1$ and $\gamma=0$ in this equation we obtain the estimate $A=2.4\times10^9$ G²/°K which is within $\sim30\%$ of the experimental value.

The results for the AF-P boundary in MnF_2, with $\mathbf{H}\|[001]$, were compared to similar data for $MnBr_2\cdot4H_2O$ ($T_N=2.13$°K), $MnCl_2\cdot4H_2O$ ($T_N=1.63$°K), and $MnCl_2\cdot4D_2O$ ($T_N=1.59$°K), all of which contain Mn^{++}. Using reduced temperatures and fields and setting $g=2.00$, the present work gives for the parameter a in Eq. (8) $a=0.068\pm0.004$. The data of Schelleng and Friedberg[12] for $MnBr_2\cdot4H_2O$ give $a=0.076$. The resonance results of Gijsman *et al.*[9] for $MnCl_2\cdot4H_2O$ give $a\cong0.063$, whereas their magnetization data give $a\cong0.073$. The recent results of Forstat *et al.*[14] for $MnCl_2\cdot4D_2O$ give $a\cong0.071$. Thus, in spite of the large variation in T_N, the parameter a is fairly constant for all these materials. Such a "law of corresponding states" is not unexpected. Assuming that $z_2|J_2|\ll z_1|J_1|$ the MFA [Eq. (9)] gives $a=0.053$ for Mn^{++} ($S=\frac{5}{2}$).

Near T_N, the MFA predicts that the AF-P boundary with $\mathbf{H}\|[100]$ is described by Eq. (25a), where the coefficient D_1 is calculated from either of Eqs. (1) through (4). Experimentally, this boundary obeys Eq. (25a) near T_N (at least approximately), but the experimental value $D_1=(1.3$ to $1.6)\times10^{-11}$ °K/G² is substantially lower than the values $D_1=(2.4$ to $4.1)\times10^{-11}$ °K/G² calculated from Eqs. (1) through (4). For the SF-P boundary with $\mathbf{H}\|[001]$, the experimental value of d^2T/dH^2 is also smaller than that predicted by the MFA.

The disagreement with the MFA can also be seen in another way. According to the MFA, the coefficient D_1 for the AF-P boundary [hereafter $D_1^{AFP}(\theta)$] varies as $(1+2\cos^2\theta)$, where θ is the angle between $\mathbf{H}$ and $\mathbf{n}$ [see Eq. (1)]. In particular, $D_1^{AFP}(90°)=(\frac{1}{3})D_1^{AFP}(0)$. Also, for the SF-P boundary with $\mathbf{H}\|\mathbf{n}$ the coefficient D_1^{SFP} should be approximately equal to $\frac{1}{3}D_1^{AFP}(0)$. Experimentally, however, $D_1^{AFP}(90°)$ and D_1^{SFP} are less than $\sim\frac{1}{10}D_1^{AFP}(0)$. For $MnCl_2\cdot4H_2O$ and $MnBr_2\cdot4H_2O$ the available data[9,13] for $D_1^{AFP}(90°)/D_1^{AFP}(0)$ and

[38] J. C. Burgiel and M. W. P. Strandberg, J. Phys. Chem. Solids **26**, 865, 877 (1965).

[39] C. Trapp, Ph.D. thesis, University of Chicago, 1963 (unpublished). See also C. Trapp and J. W. Stout, Phys. Rev. Letters **10**, 157 (1963).

[40] S. Foner, in *Magnetism*, edited by G. T. Rado and H. Suhl (Academic Press Inc., New York, 1963), Vol. I, p. 383.

$D_1^{SFP}/D_1^{AFP}(0)$ are in better agreement with the MFA.

Turning to the AF-SF transition (spin-flop transition) with $\mathbf{H}\|[001]$ we find that the results of our DMM measurements are in rough agreement with similar measurements performed eariler by de Gunzbourg and Krebs.[16] There are, however, two differences between the two sets of data. First, our values for H_{SF} are systematically lower than their values by 5–9%. In particular, our DMM measurements at 4.2°K give $H_{SF}=91\pm1$ kG whereas their value at the same temperature is $H_{SF}=96\pm3$ kG. From our ultrasonic measurements, $H_{SF}=92.4\pm0.5$ kG at 4.2°K. Magnetization measurements by Jacobs[15] gave $H_{SF}=93\pm2$ kG at 4.2°K. A second difference between our DMM data and those of de Gunzbourg and Krebs is that their results for $H_{SF}(T)/H_{SF}(0)$ increase slightly faster with temperature than ours.

We have compared our results for $H_{SF}(T)$ with those predicted by Eq. (24). Values for ω_0 were taken from the antiferromagnetic resonance data of Johnson and Nethercot[41] and from those of Burgiel and Strandberg.[38] Data for $\chi_\perp$ and $\chi_{||}$ were taken from Trapp.[39] The broken line in Fig. 6 shows the curve obtained from Eq. (24). As can be seen, there is a fairly good agreement between Eq. (24) and the experimental values, except at temperatures close to T_3 where the calculated values are significantly lower than the experimental ones. At 60°K the calculated value is ~12% lower than the experimental value, whereas at 64°K the calculated value is ~22% lower than the experimental value. It is possible that this discrepancy is due to the neglect of the field dependence of $\chi_{||}$ in the derivation of Eq. (24). Numerical calculations based on the MFA show that the field dependence of $\chi_{||}$ should increase H_{SF} by ~5% at 60°K, and by ~13% at 64°K, over and above the value given by Eq. (24).[42] [*Note added in proof*. The temperature variation of the spin-wave energy gap in MnF_2 was recently obtained from neutron diffraction measurements by M. Schulhof, P. Heller, and R. Nathans (private communication). When their preliminary values for ω_0 and Trapp's values for $\chi_{||}$ and $\chi_\perp$ are substituted into Eq. (24) one obtains good agreement with experimental values of H_{SF}, even at temperatures near T_3. Thus, the experimental evidence for the effect of the H dependence of $\chi_{||}$ on H_{SF} is inconclusive at present.]

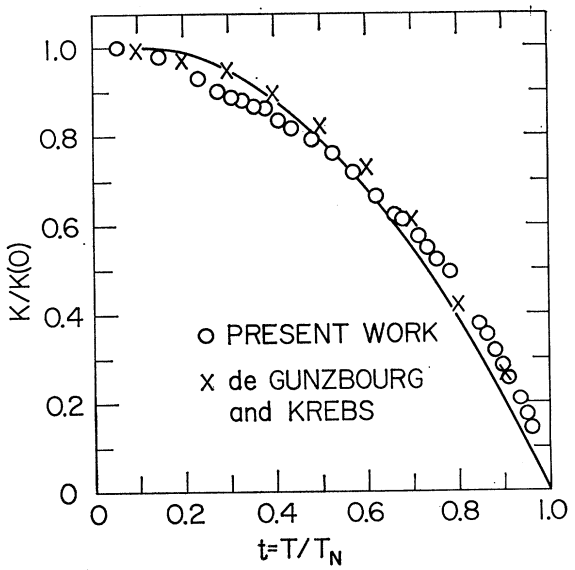

FIG. 9. The ratio $K(T)/K(0)$ deduced from our DMM data for H_{SF}, the low-field susceptibilities obtained by Trapp (Ref. 39) and Eq. (16). Also shown are the results of de Gunzbourg and Krebs (Ref. 16). The solid line represents the predictions of the MFA. A discussion of the limitations of Eq. (16) at temperatures close to T_3 is given in the text.

The temperature variation of the anisotropy energy K was deduced from the values of H_{SF} and the susceptibility data of Trapp[39] using Eq. (16). Figure 9 shows our results for $K(T)/K(0)$ together with the results of de Gunzbourg and Krebs. According to the MFA,[3] K should be proportional to the square of the sublattice magnetization at $H=0$. The sublattice magnetization is obtained by solving Eqs. (A4) and (A5) self-consistently. The predictions of the MFA for $K(T)/K(0)$ are shown in Fig. 9 as a solid line. As can be seen, there is a fairly good agreement with experiment except at temperatures close to T_3 where Eq. (16) [used in deducing $K(T)$ from experimental data] should fail because it neglects the field dependence of $\chi_{||}$. The agreement of the temperature variation of $K(T)/K(0)$ with the MFA may, however, be completely fortuitous. In calculating $K(T)$ from the MFA: (a) one lets K be proportional to the square of the sublattice magnetization at $H=0$ and (b) one solves for the sublattice magnetization using Eqs. (A4) and (A5). However, the sublattice magnetization, as inferred from NMR measurements in MnF_2, does not obey the predictions of the MFA.[4]

de Gunzbourg and Krebs compared the experimental values of $K(T)/K(0)$ with Yosida's calculations[43] and were unable to obtain good agreement. However, their comparison is unjustified because Yosida's calculations apply to the case of a single-ion anisotropy (of the form DS_z^2) and not to the anisotropy in MnF_2, which arises mainly from magnetic dipole-dipole interaction.[24] Theoretically, the single-ion anisotropy has a different temperature dependence than that of the magnetic dipole-dipole anisotropy.[3,44]

ACKNOWLEDGMENTS

We wish to thank A. Misetich for computer calculations and many informative discussions, L. G. Rubin

[41] F. M. Johnson and A. H. Nethercot, Jr., Phys. Rev. **104**, 847 (1956); **114**, 705 (1959).

[42] A. Misetich (private communication).

[43] K. Yosida, Progr. Theoret. Phys. (Kyoto) **6**, 691 (1951).

[44] M. Tachiki and T. Nagamiya, J. Phys. Soc. Japan **13**, 452 (1958).

for considerable advice in thermometry, D. R. Nelson for programming the least-squares fits, E. J. Alexander, C. F. Bir, and C. Beaton for orienting the single crystals, and V. Diorio and W. G. Fisher for technical assistance.

APPENDIX: AF-P BOUNDARIES CALCULATED FROM MFA

We consider a uniaxial antiferromagnet, of the easy-axis type, with an anisotropy interaction which is very small compared to the exchange interaction. We assume that there are two sublattices and that the intrasublattice exchange interaction is negligible compared to the intersublattice exchange interaction.

1. H Normal to Preferred Axis

The effective field $\mathbf{H}_{eff}^{(1)}$ on sublattice No. 1 is given by

$$H_{eff}^{(1)}=\mathbf{H}-\lambda\mathbf{M}_2, \tag{A1}$$

where λ is the intersublattice exchange constant which is related to J_1 by the expression[45]

$$\lambda=\frac{2z_1|J_1|}{Ng^2\mu_B^2}. \tag{A2}$$

Here N is the number of spins per sublattice per cm^3. The equilibrium position of the sublattice magnetizations in the AF phase is determined by the condition that $\mathbf{H}_{eff}^{(1)}$ is parallel to $\mathbf{M}_1$, and similarly for $\mathbf{H}_{eff}^{(2)}$.

The equilibrium configuration of $\mathbf{M}_1$ and $\mathbf{M}_2$ is shown in Fig. 10. Geometric considerations lead to the relations

$$\sin\delta=H/2\lambda M_1, \tag{A3}$$

$$H_{eff}^{(1)}=H_{eff}^{(2)}=\lambda M_1=\lambda M_2. \tag{A4}$$

The magnitude of M_1 (or M_2) is determined by the relation

$$M_1=M(0,0)B_S(g\mu_BSH_{eff}^{(1)}/kT), \tag{A5}$$

where $B_S(x)$ is the Brillouin function for the spin S, and $H_{eff}^{(1)}$ is given by Eq. (A4). Since Eqs. (A4) and (A5) also determine M_1 (or M_2) at $H=0$, it follows that the magnitude of the sublattice magnetization $M_1(H,T)$ does not vary with H in the AF state, i.e.,

$$M_1(H,T)=M_1(0,T), \tag{A6}$$

and similarly for M_2.

As H increases $\mathbf{M}_1$ and $\mathbf{M}_2$ rotate, without a change in their magnitude, until δ is equal to 90°. When $\delta=90°$, $\mathbf{M}_1$ and $\mathbf{M}_2$ are equal to each other which is the characteristic of the paramagnetic phase. The field at the AF-P transition is determined therefore by the condition $\sin\delta=1$, or

$$H=2\lambda M_1. \tag{A7}$$

[45] J. S. Smart, *Effective Field Theories of Magnetism* (W. B. Saunders Co., Philadelphia, 1966).

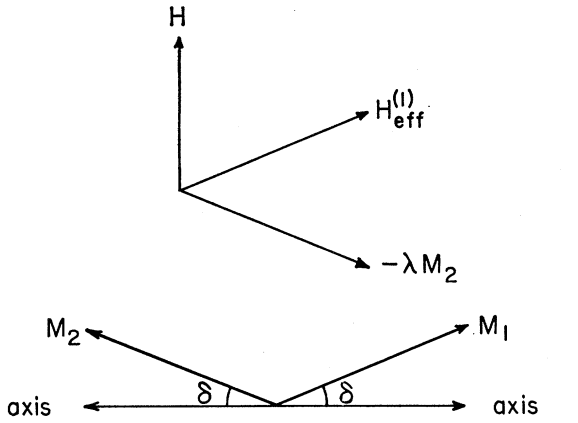

FIG. 10. The equilibrium orientations of the sublattice magnetizations $\mathbf{M}_1$ and $\mathbf{M}_2$ in the AF phase when $\mathbf{H}$ is normal to $\mathbf{n}$. Also shown are the various fields which act on sublattice No. 1.

Using Eq. (A6) the AF-P boundary is given by

$$H=2\lambda M_1(0,T). \tag{A8}$$

Equation (A8) applies at any temperature below T_N. For T just below T_N, $M_1(0,T)$ is given by[45]

$$M_1(0,T)=Ng\mu_BS[10(S+1)^2/3(2S^2+2S+1)]^{1/2}(1-T/T_N)^{1/2}. \tag{A9}$$

The Néel temperature is given by

$$kT_N=\tfrac{2}{3}S(S+1)z_1|J_1|. \tag{A10}$$

Combining Eqs. (A8)–(A10) we obtain

$$T_N-T=\frac{(2S^2+2S+1)g^2\mu_B^2H^2}{80S(S+1)kz_1|J_1|}. \tag{A11}$$

Using Eq. (A10), Eq. (A11) can be rewritten as

$$T_N-T=\frac{(2S^2+2S+1)g^2\mu_B^2H^2}{120k^2T_N}. \tag{A12}$$

To derive Eq. (A12) for the AF-P transition we used the solution for $M_1(H,T)$ *in the AF phase* [Eqs. (A6) and (A9)] and imposed the condition (A7) for the transition. It is instructive to rederive Eq. (A12) by considering $M_1(H,T)$ *in the P phase* and then imposing condition (A7) for the transition. In the P phase $\mathbf{M}_1=\mathbf{M}_2$ so that

$$\mathbf{H}_{eff}^{(1)}=\mathbf{H}-\lambda\mathbf{M}_1. \tag{A13}$$

M_1 is then given by the self-consistent solution of the equation

$$M_1=Ng\mu_BSB_S[g\mu_BS(H-\lambda M_1)/kT]. \tag{A14}$$

We now impose condition (A7) for the transition and

use the expansion

$$B_S(x)=\frac{(S+1)}{3S}x-\frac{(S+1)(2S^2+2S+1)}{90S^3}x^3+O(x^5) \tag{A15}$$

for $x\ll 1$. This gives

$$M_1=\frac{Ng^2\mu_B{}^2S(S+1)\lambda M_1}{3kT}\left[1-\frac{(2S^2+2S+1)g^2\mu_B{}^2H^2}{120k^2T^2}\right], \tag{A16}$$

where we have neglected terms of order x^5 or higher in the expansion (A15). Using Eqs. (A2) and (A10) one then obtains

$$T_N-T=\frac{(2S^2+2S+1)g^2\mu_B{}^2H^2(T_N/T)^2}{120k^2T_N}. \tag{A17}$$

In solving for T_N-T we have been retaining terms up to order $T_N(g\mu_BSH/kT_N)^2$. Within this approximation we may replace the ratio (T_N/T) *on the right side* of Eq. (A17) by unity and obtain Eq. (A12).

2. H Parallel to Preferred Axis

We assume that $\mathbf{H}\|\mathbf{n}$ and that $T_3<T<T_N$. In the AF phase the magnetizations of the two sublattices are parallel or antiparallel to $\mathbf{n}$ and are determined by the self-consistent solution to the pair of equations

$$\mathbf{n}\cdot\mathbf{M}_1(H,T)=Ng\mu_BSB_S[g\mu_BS(H-\lambda\mathbf{n}\cdot\mathbf{M}_2)/kT] \tag{A18a}$$

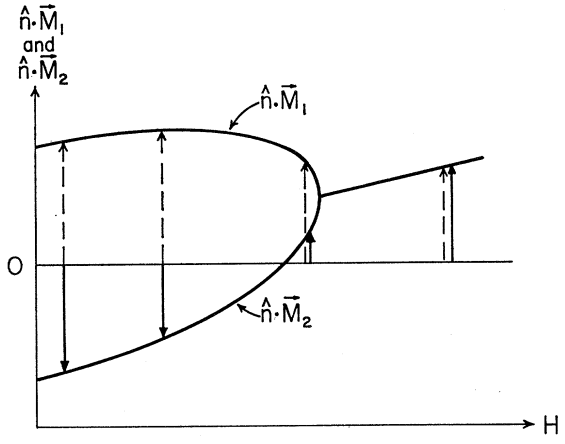

FIG. 11. The solid curves show a typical variation of $\mathbf{n}\cdot\mathbf{M}_1$ and $\mathbf{n}\cdot\mathbf{M}_2$ with H, at $T_3<T<T_N$ and with $\mathbf{H}\|\mathbf{n}$. The broken and solid arrows represent $\mathbf{M}_1$ and $\mathbf{M}_2$, respectively, with $\mathbf{n}$ pointing upward. The AF-P transition occurs at the lowest field for which $\mathbf{M}_1$ is equal to $\mathbf{M}_2$.

and

$$\mathbf{n}\cdot\mathbf{M}_2(H,T)=Ng\mu_BSB_S[g\mu_BS(H-\lambda\mathbf{n}\cdot\mathbf{M}_1)/kT]. \tag{A18b}$$

This pair of equations can be solved numerically using a computer. A typical variation of $\mathbf{n}\cdot\mathbf{M}_1$ and $\mathbf{n}\cdot\mathbf{M}_2$ with H at a temperature just below T_N is shown in Fig. 11.[42]

To obtain an analytical solution for the AF-P boundary we note that in fields near the transition field $\mathbf{n}\cdot\mathbf{M}_1=M_1$ and $\mathbf{n}\cdot\mathbf{M}_2=M_2$ (see Fig. 11). When H is lower than the transition field by an infinitesimal amount, the difference M_1-M_2 is obtained from Eqs. (A18), viz.,

$$M_1-M_2=(Ng^2\mu_B{}^2S^2\lambda/kT)\times(M_1-M_2)[dB_S(x)/dx]. \tag{A19}$$

In Eq. (A19), the derivative $dB_S(x)/dx$ is evaluated at that value which the argument of the Brillouin function in Eqs. (A18) takes at the transition. Using Eq. (A15) one then obtains for T just below T_N

$$1=[Ng^2\mu_B{}^2S(S+1)\lambda/3kT]\times[1-(2S^2+2S+1)g^2\mu_B{}^2(H-\lambda M_t)^2/10k^2T^2], \tag{A20}$$

where M_t is the sublattice magnetization at the AF-P transition. Using Eqs. (A2) and (A10) one obtains

$$T_N-T=\frac{(2S^2+2S+1)g^2\mu_B{}^2(H-\lambda M_t)^2T_N}{10k^2T^2}. \tag{A21}$$

At the AF-P transition $M_1=M_2=M_t$ and M_t satisfies the equation

$$M_t=Ng\mu_BSB_S[g\mu_BS(H-\lambda M_t)/kT], \tag{A22}$$

which for T near T_N and for $g\mu_BSH\ll kT_N$ has the approximate solution[46]

$$M_t=H/2\lambda. \tag{A23}$$

Substituting Eq. (A23) into Eq. (A21) and replacing T on the right of Eq. (A21) by T_N, we obtain

$$T_N-T=\frac{(2S^2+2S+1)g^2\mu_B{}^2H^2}{40k^2T_N} \tag{A24}$$

for the AF-P boundary at T just below T_N. Using Eq. (A10), Eq. (A24) can be rewritten in the form

$$T_N-T=\frac{3(2S^2+2S+1)g^2\mu_B{}^2H^2}{80S(S+1)kz_1|J_1|}. \tag{A25}$$

[46] Equation (A23) holds *approximately* throughout the P phase provided that T is near T_N and that $g\mu_BSH\ll kT_N$. When $\mathbf{H}\perp\mathbf{n}$ Eq. (A23) holds *exactly* at the AF-P transition [see Eq. (A7)].